RSC Advances

ROYAL SOCIETY OF CHEMISTRY

www.rsc.org/advances

Structural and magnetic properties of GaN/Mn nanopowders prepared by an anaerobic synthesis route

Mariusz Drygas,[1a] Jerzy F. Janik,[1a]* Miroslaw M. Bucko,[1b] Jacek Gosk,[2,3] Andrzej Twardowski[2]*

[1]AGH University of Science and Technology, [a]Faculty of Energy and Fuels, [b]Faculty of Materials Science and Ceramics; al. Mickiewicza 30, 30-059 Krakow, Poland.
[2]University of Warsaw, Faculty of Physics; ul. Pasteura 5, 02-093 Warszawa, Poland.
[3]Warsaw University of Technology, Faculty of Physics, ul. Koszykowa 75, 00-662 Warszawa, Poland

*Corresponding authors: janikj@agh.edu.pl; andrzej.twardowski@fuw.edu.pl

Abstract. A new oxygen-free molecular precursor system based on (i) ammonolysis in liquid NH_3 of selected mixtures of gallium tris(dimethyl)amide $Ga(NMe_2)_3$ and manganese bis(trimethylsilyl)amide $Mn[N(SiMe_3)_2]_2$ (Me = CH_3, initial Mn-contents = 0.1, 5, 20, 50 at.%) followed by (ii) pyrolysis under ammonia at 500, 700, and 900 °C afforded a range of nanocrystalline powders in the GaN/Mn system. The nanopowders were characterized mainly by powder XRD diffractometry, FT-IR spectroscopy, Raman spectroscopy, SEM/EDX morphology examination, and XRF elemental analysis. Magnetization measurements in function of magnetic field and temperature were carried out with a SQUID magnetometer. Structurally, the materials were shown to be single-phases based on the gallium nitride lattice. The presence of small quantities of residual amorphous Mn/N/Si/C species due to an incomplete transamination/removal of the trimethylsilylamide groups during ammonolysis was deduced from the XRF, FT-IR, and magnetization data. Magnetic properties for all nanopowders consistently pointed out to a paramagnetic GaMnN phase with antiferromagnetic interactions among Mn-centers that under favorable circumstances reached the level of up to 3.8 at.% Mn in the GaN lattice. The paramagnetic phase is accompanied by a residual antiferromagnetic phase due to a facile oxidation in air of amorphous Mn-containing by-products.

This paper is dedicated to Professor Robert T. Paine, UNM, Albuquerque, New Mexico, USA, on the occasion of his retirement.

Keywords: diluted magnetic semiconductor, gallium nitride, manganese, spintronics.

1. Introduction

Gallium nitride GaN suitably doped with a magnetic transition metal (TM = Mn, Fe, Cr, etc.), that can be abbreviated as GaN/TM or GaTMN, has been anticipated for many promising applications as a dilute magnetic semiconductor DMS. The DMS materials are crucial in spintronics – spin based electronics which utilize both the semiconducting and magnetic properties residing in one material and some recent contributions and comprehensive reviews of the subject are available.[1] The known DMS materials are usually produced either as kinetically-stabilized TM-doped thin films or monocrystals. In this regard, sintered GaN-based DMS ceramics prepared from nanopowders can, potentially, be a new convenient form of such materials for many challenging applications.[2] The reproducible preparation and characterization of GaN-based DMS nanopowders are, therefore, indispensable for further progress in this area.

The preparation of GaN-based thin films and monocrystals doped with selected transition metals including Mn was the subject of studies carried out by some of the authors of this report.[3] The attention was also given to dope the nitride microcrystalline powders *via* the ammonothermal synthesis.[4] GaN/Mn nanocrystalline powders were previously prepared by some of us using both the aerosol-assisted and anaerobic synthesis methods. The aerosol-assisted synthesis used the readily available oxygen-bearing nitrates of gallium and manganese and yielded some Mn-centers incorporated in the GaN lattice but it was plagued by the formation of a residual antiferromagnetic manganese oxide MnO by-product.[5] The anaerobic synthesis dwelled on the anticipated incorporation of Mn-centers into the gallium imide framework, the latter formed by transamination/deamination chemistry in the oxygen-free gallium (III) tris(dimethyl)amide/ammonia reaction system, $Ga(NMe_2)_3/NH_3$ (Me = CH_3).[6] Based on magnetization measurements, up to 3.5 % of Mn-centers were incorporated in the hexagonal GaN nanopowders. However, the use of the oxygen-bearing manganese (III) acetylacetonate dopant resulted again in some antiferromagnetic MnO impurity.

There is only a handful of other reports concerned with magnetic doping of GaN powders. In one report, Mn-doped GaN microcrystalline powders containing *ca.* 0.1 % of Mn were made by solid-state metathesis using Mn, Li_3N, and Ga_2O_3 as precursors.[7] In another study, similar powders, claimed with up to 7 at.% of incorporated Mn, were prepared in the gallium (III) nitrate/manganese (II) nitrate precursor system *via* conversion to oxides and, finally, reactions with ammonia at elevated temperatures.[8] In a different approach, magnetic

GaN/GaN:Mn core/shell nanowires were synthesized in a multistep process that included GaN nanowire preparation by vapor phase MOCVD and the nanowire surface modification by chemical vapor transport with the use of the Ga and $MnCl_2$ precursor mixture.[9] Modifications of a route to GaN nanowires, based on the use of GaN powders and $MnCl_2$, resulted in hexagonal GaN-based nanowires modified in bulk with Mn up to 10 %.[10]

Looking back at the transamination/deamination chemistry explored earlier by us, one can envision that the application of an oxygen-free bimetallic precursor system such as made of gallium (III) tris(dimethyl)amide/manganese (II) bis(dimethyl)amide, $Ga(NMe_2)_3/Mn(NMe_2)_2$, would create advantageous conditions for mixed organometallic species and, after reactions with ammonia, it would favor the evolution of Ga-N-Mn-N linkages whereas circumvent the formation of manganese oxygen by-products. This kind of chemistry was earlier confirmed by us in the system gallium (III) tris(dimethyl)amide/aluminum (III) tris(dimethyl)amide which upon reactions with ammonia afforded solid solutions of GaAlN at high temperatures.[11] However, manganese (II) bis(dimethyl)amide is unknown and our initial attempts to make it *via* metathesis of MnX_2 (X = Cl, Br) and $LiNMe_2$ have missed the target. On the other hand, a related silylated amine derivative, *i.e.*, manganese (II) bis(trimethylsilyl)amide $Mn[N(SiMe_3)_2]_2$, is available from the metathetical reaction in the system MnX_2 (X = Cl, Br)/$LiN(SiMe_3)_2$.[12] In general, both the metal silylamide and metal regular amide derivatives are thought to undergo similar ammonolysis/nitridation reactions with the evolution of volatile $HN(SiMe_3)_2$ or $HNMe_2$, respectively, and NH_3, and the formation of a nitride with increasing temperatures. This will be true if the crucial ammonolysis step results in complete transamination and efficient removal of the amine groups from the system. Otherwise, the final materials can be contaminated with silylamine group decomposition by-products, mainly, TM-N-Si-C species.

First, for the Mn-silylamide derivative, one can expect under favorable conditions a temperature-driven idealized reaction sequence shown below.[13]

$$Mn[N(SiMe_3)_2]_2 + 2NH_3 \rightarrow Mn(NH_2)_2 \text{ (amide)} + \uparrow 2HN(SiMe_3)_2 \quad \text{transamination}$$

$$Mn(NH_2)_2 \rightarrow Mn(NH) \text{ (imide)} + \uparrow NH_3 \quad \text{deamination}$$

$$3Mn(NH) \rightarrow \{\text{-Mn-N-Mn-N-Mn-}\} \text{ (nitride)} + \uparrow NH_3 \quad \text{deamination}$$

Second, gallium tris(dimethyl)amide is known to react with NH_3 paralleling the chemistry above and forming the polymeric gallium imide at room temperature.[11,14] The imide upon nitriding pyrolysis at elevated temperatures is then converted to pure GaN nanopowders. The overall pathway constitutes a reference precursor system in the current study.

$Ga(NMe_2)_3 + 3NH_3 \rightarrow Ga(NH_2)_3$ (amide) $+ \uparrow 3HNMe_2$ transamination

$2Ga(NH_2)_3 \rightarrow 2/n\{Ga(NH)_{3/2}\}_n$ (imide) $+ \uparrow 3NH_3$ deamination

$2/n\{Ga(NH)_{3/2}\}_n \rightarrow$ {-Ga-N-Ga-N-} (nitride) $+ \uparrow NH_3$ deamination

Therefore, the combination of managanese (II) bis(trimethylsilyl)amide and gallium (III) tris(dimethyl)amide provides a viable precursor system for the formation of mixed metal-nitride linkages already at the bimetallic precursor level, which creates advantageous conditions for incorporating Mn-centers in the evolving GaN lattice at higher temperatures.

In this study, we utilized the bimetallic system $Ga(NMe_2)_3/Mn[N(SiMe_3)_2]_2$ with various initial Ga:Mn atomic ratios and conversion temperatures to promote the GaN/Mn powder formation under a broad range of conditions. The resulting nanopowders were thoroughly characterized including detailed measurements of their magnetic properties.

2. Experimental

Synthesis. The synthesis method used to make GaN/Mn powders was based on the reported anaerobic preparation of pure nanocrystalline gallium nitride GaN from polymeric gallium imide $\{Ga(NH)_{3/2}\}_n$.[14] To achieve the synthesis of various Mn-doped materials while conforming to the basic procedure, two major mixtures of $Ga(NMe_2)_3$ and $Mn[N(SiMe_3)_2]_2$ with the initial Mn-contents of 5 and 20 at.% were employed. Also, one precursor mixture was made with 0.1 at.% Mn and another one with 50 at.% Mn to check the extreme metals compositions. Additionally, a sample with 10 at.% Mn was prepared to investigate a modification of the crucial transamination stage. For the 0.1, 20, and 50 at.% Mn-contents, a two-stage pyrolysis of the respective room temperature precursor under a NH_3 flow, 0.5 L/min, was performed: first stage, 18 h at 150 ºC and second stage, 4 h at 500, 700 or 900 °C to afford gray-beige to gray-brownish final powders. For the 5 at.% Mn-content bimetallic precursor, one-stage pyrolysis under a NH_3 flow, 0.5 L/min, 4 h at 500, 700 or 900 °C was carried out to yield similarly colored powders. For this Mn-content, one additional sample was prepared at 500 °C *via* the two-stage pyrolysis. The resulting samples reflected both the various initial proportions of Mn and the range of pyrolysis temperatures as the predominant experimental factors. The synthesis routes are shown in Figure 1.

Sample labeling. The samples were labeled to show the basic parameters of their preparation, *i.e.*, the initial Mn-content and the temperature pyrolysis levels. For example, the label 20Mn-150/700 refers to the powder from the bimetallic precursor containing 20 at.% Mn and

pyrolyzed, first, at 150 ºC followed by pyrolysis at 700 ºC whereas 5Mn-900 describes the powder from the relevant precursor with 5 at.% Mn which was pyrolyzed only at 900 ºC.

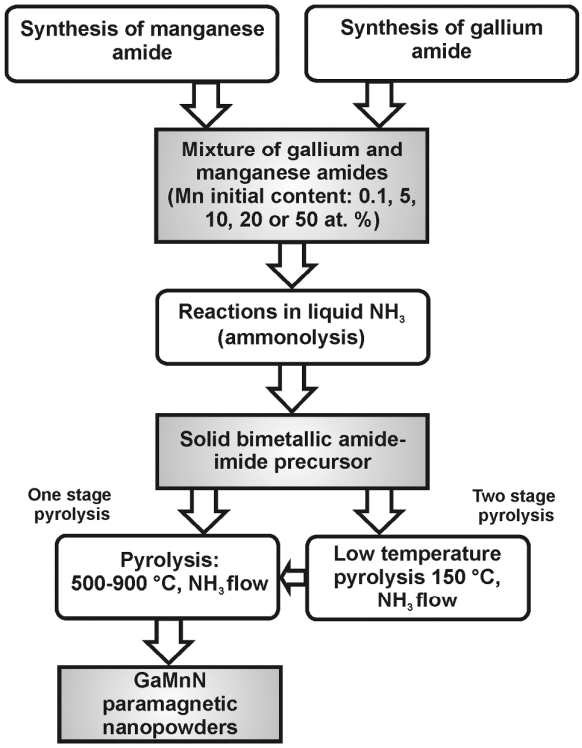

Fig. 1. Synthesis of GaN/Mn nanopowders in the system $Ga(NMe_2)_3/Mn[N(SiMe_3)_2]_2/NH_3$.

Characterization. All product powders were characterized by the standard powder XRD technique with a X'Pert Pro Panalytical diffractometer (Cu K_α source; 2Θ=20–80°). Average crystallite sizes were evaluated from the Scherrer's equation applying the Rietveld refinement method. For the evaluation, changes of the line profile parameters compared to a standard sample were utilized. Our standard was a polycrystalline alumina sintered body with an average grain size over 5 μm subjected to stress relief annealing. The profile parameters depend on the instrument settings used for data collection and on the profile function used for the refinement. In our analysis the full Voight function was used to describe the profile of the measured diffraction lines. The total profile width is a convolution of the Gaussian profile part and of the Lorentzian profile part and these parts are combined numerically. In such a method, the full width at half-maximum (fwhm) is only one of several fitted parameters. X-ray fluorescence XRF determinations were performed on PANalytical WDXRF Axios mAX spectrometer equipped with a 4 KW Rh lamp. FT-IR spectra for solids (KBr pellets) were collected on a Nicolet 380 spectrometer. Micro-Raman analysis was done by HORIBA LabRAM HR spectrometer with spectral resolution 0.5 cm^{-1}. SEM/EDX study was performed

using a Hitahi Model S-4700 scanning electron microscope. Magnetization of the samples was measured as a function of magnetic field (up to 7 Tesla) and temperature (2-400 K) using a superconducting quantum interference device (SQUID) magnetometer. The powder samples were placed in capsules showing controlled diamagnetic signal. To reduce the ratio of holder signal to signal of the measured sample, the sample mass was maximized with respect to the upper limit of the SQUID operation range.

3. Results and Discussion

The idea to use the bimetallic system $Ga(NMe_2)_3/Mn[N(SiMe_3)_2]_2/NH_3$ (Me = CH_3) to make GaN/Mn powders *via* thermally-driven transamination/deamination chemistry has a firm support from the available data on the related conversions as already discussed.[11,13,14] The crucial transamination step in this precursor system is usually incomplete and the presence of some contaminant amorphous N-Si-C species from the thermal decomposition of residual $N(SiMe_3)_2$ groups cannot be excluded. Namely, at sufficiently high temperatures, the competing decomposition pathways start to prevail and lead, first, to polymeric N-Si-C species and, eventually, to silicon nitride and/or silicon carbide by-products.[15,16] Al this means that the application of $Mn[N(SiMe_3)_2]_2$ in the transamination/deamination reactions can be, potentially, a source of this kind of contaminations. It can especially be true in this study where excess quantities of the manganese precursor are purposely applied.

In order to evaluate the suitability of pure $Mn[N(SiMe_3)_2]_2$ to form nitrides, a study of its transamination/deamination chemistry was carried out and the results will be published elsewhere.[17] In summary of this research, the reactions of the compound with liquid NH_3 appear to result in an incomplete ammonolysis and yield at room temperature only partially transaminated precursor containing mostly the $-NH_2$ and $-N(SiMe_3)_2$ functionalities. The reactions of this precursor with ammonia gas already at the temperature as low as 150 ºC yield pure nanocrystalline manganese nitride η-Mn_3N_2. One could conclude, therefore, that upon suitable adjustments the manganese compound would undergo equally efficient reactions with ammonia in the bimetallic system $Ga(NMe_2)_3/Mn[N(SiMe_3)_2]_2$.

FT-IR spectroscopy of precursors. In Figure 2, the FT-IR spectra for the reference monometallic reaction systems, $Ga(NMe_2)_3$/liquid NH_3 and $Mn[N(SiMe_3)_2]_2$/liquid NH_3, and for the 5, 10, 20, and 50 at.% Mn-content/liquid NH_3 bimetallic reaction systems are shown. The FT-IR spectrum for product from the system $Ga(NMe_2)_3$/liquid NH_3 (upper left) is typical for polymeric gallium imide with residual NMe_2 groups.[14] The medium intensity broad bands

at 3136 cm^{-1} and 1506 cm^{-1} are for N-H vibrations in the imide groups Ga-NH-Ga, and a strong broad peak at 557 cm^{-1} is for Ga-N stretches in the Ga-N lattice. The remaining peaks reflect the residual NMe_2 groups.

The FT-IR spectrum for an insoluble product (upper right), which is isolated at room temperature from the reaction of pure $Mn[N(SiMe_3)_2]_2$ in liquid NH_3, confirms its incomplete transamination as discussed earlier. There are two peaks at 3332 and 3267 cm^{-1} that are assigned to N-H stretches and one peak at 1564 cm^{-1} assigned to N-H deformation in the Mn-NH_2 amide groups. The remaining peaks are assigned to the unconverted Mn-$N(SiMe_3)_2$ groups. Especially, a pretty strong peak at *ca.* 1250 cm^{-1} is diagnostic for $SiMe_3$ groups. In conclusion, the product appears to be best approximated as $\{Mn[N(SiMe_3)_2]_x(NH_2)_{2-x}\}$.

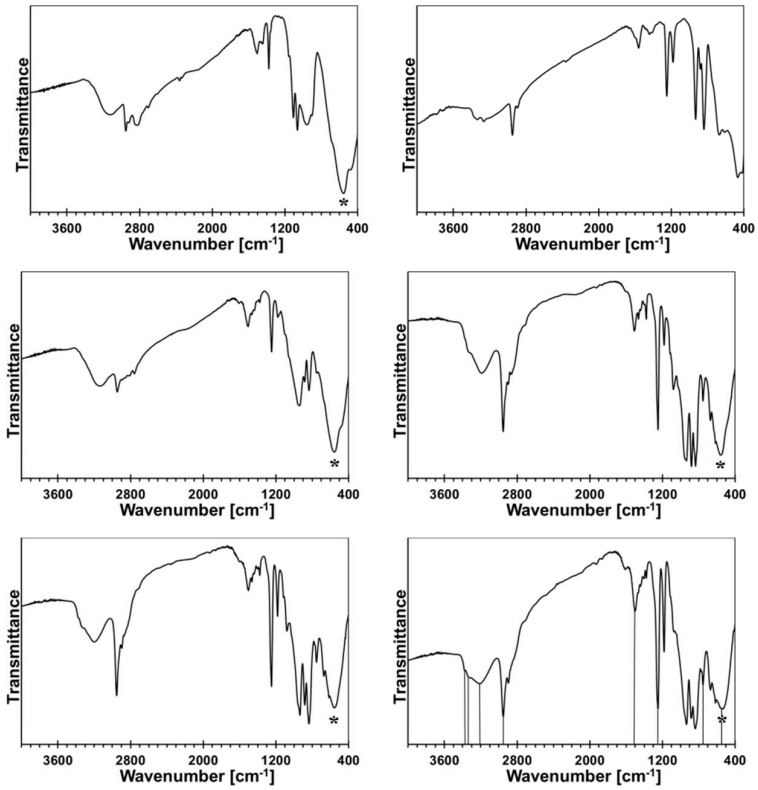

Fig. 2. FT-IR spectra of mono and bimetallic precursors after reactions with liquid NH_3: upper left – $Ga(NMe_2)_3$/liq. NH_3, upper right – $Mn[N(SiMe_3)_2]_2$/liq. NH_3, middle left – 5 at.% Mn, middle right – 10 at.% Mn, lower left – 20 at.% Mn, lower right – 50 at.% Mn. Asterisk shows Ga-N stretch, vertical lines in the lower right are guides to the eye for important bands.

The FT-IR spectra for the 5 (middle left), 10 (middle right), 20 (lower left), and 50 at.% Mn (lower right) are all consistent in that the relative intensities of the peaks assigned to residual $N(SiMe_3)_2$ groups increase in a systematic way with the higher and higher proportion

of initial Mn. This is best seen when comparing the peaks at *ca.* 2950/2900 and 1250 cm^{-1} for the C-H stretches and Si-CH_3 deformation in the Mn-$N(SiMe_3)_2$ groups, respectively, to the strong peak at *ca.* 550-560 cm^{-1} for the Ga-N stretches. The predominant peaks for N-H species become now characteristic of the imide type groups, *i.e.*, at *ca.* 3190-3220 and 1500-1510 cm^{-1}. This suggests that a significant proportion of the Mn-NH_2 groups reacts with *in statu nascendi* Ga-NH_2 to form Ga-NH-Mn linkages according to Ga-NH_2 + H_2N-Mn → {Ga-N(H)-Mn} + ↑NH_3. In this regard, a new peak of weak to medium intensity at 754 cm^{-1} is detected for all the bimetallic precursors. The peak is absent in the infrared spectra of both pure metal-derived precursors. We assign this peak tentatively to Mn-N stretches in the bimetallic {Ga-N(H)-Mn}-type of species.

Some of the bimetallic precursors were pyrolyzed under ammonia at 150 ºC for 18 h before the pyrolysis at higher temperatures. This was done to promote an advantageous removal of the residual $N(SiMe_3)_2$ groups *via* transamination. This temperature is known to be safely below a range of $SiMe_3$ thermal decomposition starting at 250-300 ºC.[15,16] The FT-IR spectra for the 10, 20, and 50 at.% Mn precursors of this type are shown in Figure 3.

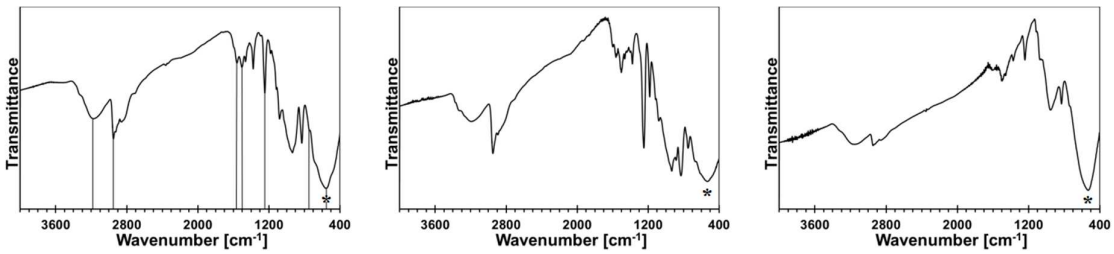

Fig. 3. FT-IR spectra of bimetallic precursors after reactions in liquid NH_3 that were additionally pyrolyzed under ammonia at 150 °C, 18 h: left – 10 at.% Mn, middle – 20 at.% Mn, right – 50 at.% Mn. Asterisk shows Ga-N stretch, vertical lines in the left are guides to the eye for important bands.

The major conclusion that is drawn from comparison of these spectra with the respective spectra for their starting counterparts in Fig. 2 is that the pyrolysis under ammonia at 150 ºC results in further transamination/removal of the $N(SiMe_3)_2$ groups but still some of them are retained. This is clearly seen by comparing the relative intensities of the C-H stretch in Si-CH_3 at 2950 cm^{-1} to the imide N-H stretch at 3170-3200 cm^{-1} or the Si-CH_3 deformation at 1245-1250 cm^{-1} to the Ga-N stretch at 560 cm^{-1} in the related spectral pairs. Also, a detailed inspection of the spectra supports the notion that the progressing transamination of the Mn-$N(SiMe_3)_2$ groups during the 150 ºC-pyrolysis results in increasing quantities of the Mn-NH_2

groups but does not have any significant impact on an additional Ga-NH-Mn linkage formation as judged by the relative intensities of the diagnostic peak at *ca.* 750 cm^{-1}.

SEM/EDX examination. The morphology of the powders was examined by SEM/EDX and typical images are shown in Figures 4-6. In Figure 4, the pictures for the initially 5 at.% Mn-content materials pyrolyzed at 500, 700, and 900 ºC are included. In all these cases, a similar grain-type morphology of aggregates in confirmed. The element mapping confirms in all cases that both Ga and Mn are homogenously dispersed. An attempted mapping for Si was within a level of background noise.

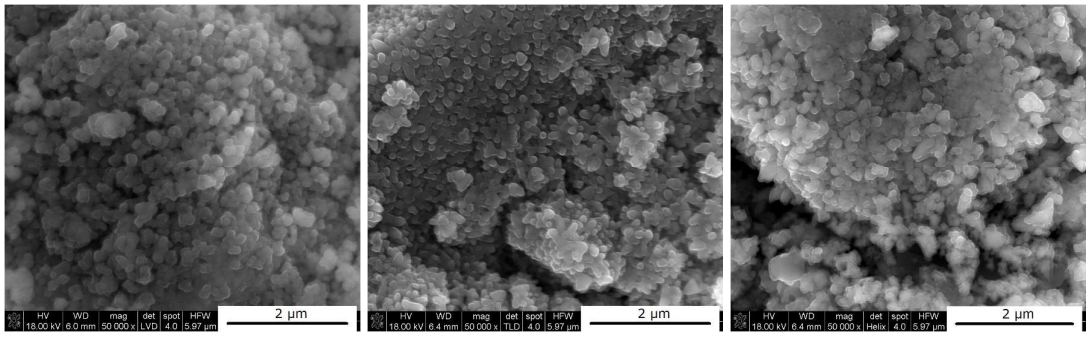

Fig. 4. SEM images of powders with initial 5 at.% Mn-content: left – 5Mn-500, middle – 5Mn-700, right – 5Mn-900.

Figure 5 shows the SEM pictures for all pyrolyzed powders with the initial 20 at.% Mn-content. The overall appearance of the large pieces seen at the relatively low magnification suggests a transient gluey state of the precursor before full solidification to blocky chunks, especially, at 500 and 700 ºC. The evolution of regularly shaped crystallites with increasing pyrolysis temperatures is clearly evident. This is already visible at 700 ºC (middle picture) and takes a form of heterogenous areas with distinct morphologies at 900 ºC (right picture). In the latter, a columnar growth of elongated sharp-ended microcrystallites can be compared with a grainy texture of the large bulk pieces. EDX spot analyses, labeled with the numbers in white, were carried out for distinct morphological features in the samples. Due to superposition of neighboring particles and varying sample thicknesses, only semi-quantitative results were obtained. For 20Mn-150/500 (Fig. 5, left), smooth and solid area 1 is characteristic of the largest Mn-content among the analyzed spots whereas area 3 in the morphologically different piece has this content lower by one order of magnitude relative to Ga. For 20Mn-150/700 (Fig. 5, middle), spot 1 in the grainy aggregate shows a similar Ga/Mn

ratio compared to spot 1 in the previously discussed sample, and spot 2 in an apparently blocky crystallite is significantly enriched in Mn, which indicated specific phase evolution and separation after pyrolysis at 700 °C. This phenomenon is clearly seen in sample 20Mn-150/900 from yet higher temperature pyrolysis at 900 °C (Fig. 5, right). The sharp-ended microcrystallites analyzed in spot 1 show a lower Mn-content than the blocky aggregate in spot 2. It is also found that the increased proportions of Mn were frequently associated with higher proportions of Si, the latter element seen at the relatively low levels in all samples.

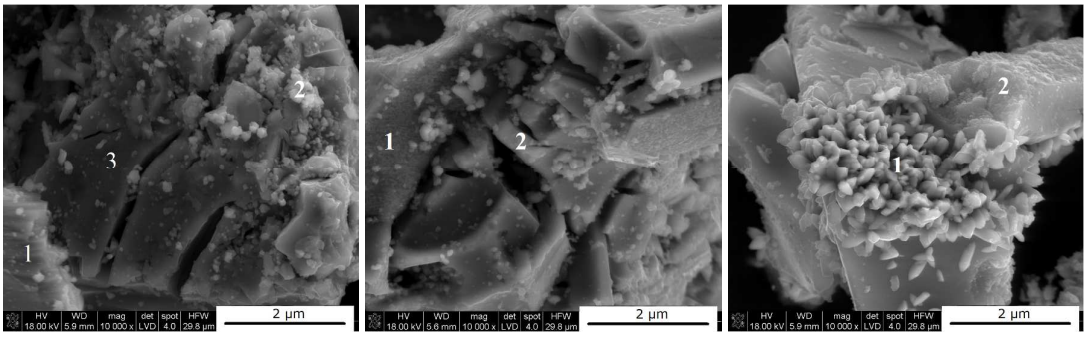

Fig. 5. SEM images of powders with initial 20 at.% Mn-content: left – 20Mn-150/500, middle – 20Mn-150/700, right – 20Mn-150/900. The numbers in white show morphologically different areas analyzed by EDX.

Two bimetallic precursors with the extreme Mn-contents of 0.1 and 50 at.% were pyrolyzed under ammonia at 900 °C. The SEM images of the resulting powders (not shown) confirmed for 0.1Mn-150/900 the homogenous grainy morphology well compared with the product from the respective 5 at.% Mn-content conversion (Fig. 4, right). For 50Mn-150/900, large microcrystallites were embedded in the agglomerated matrix of much smaller particles. For this material, the EDX analyses showed increased proportions of Mn and Si in the large crystallites compared with the bulky matrix.

The EDX mapping was done for a large inhomogeneous piece in 50Mn-150/900 and the results are shown in Figure 6. Generally, there are regions associated mostly with a solid crust with well correlated Si and Mn element distributions but there are also small areas where Mn does not correlate either with Si or Ga as, for example, shown with the ellipse. There are also features that can be attributed to some combination of the Mn and Si elements with no Ga contribution, which are enclosed in the black and white rectangle. These results point out to a complex composite make-up of the powder.

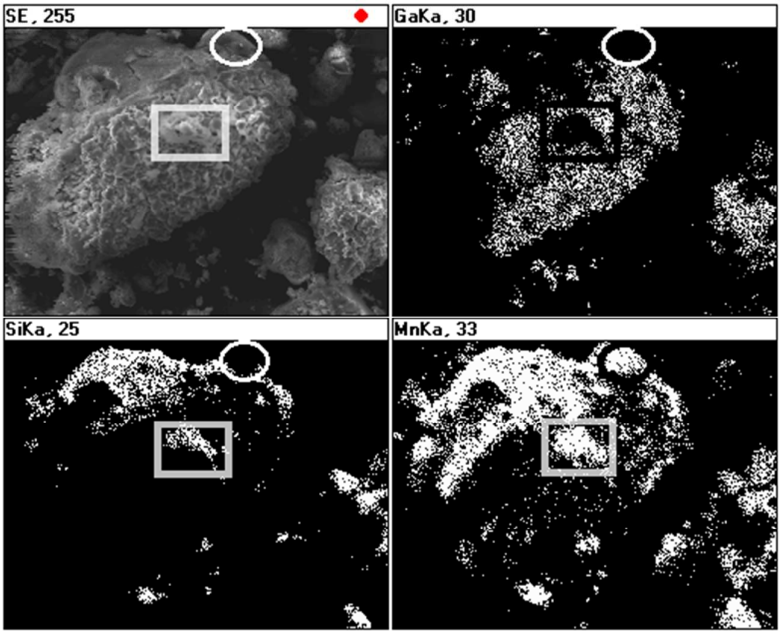

Fig. 6. SEM/EDX element mapping for powder with initial 50 at.% Mn-content: upper left – low-magnification image for 50Mn-150/900, upper right – Ga-distribution, lower left – Si-distribution, lower right – Mn-distribution.

XRF analysis. The SEM/EDX analyses were consistent with incomplete transamination chemistry during ammonolysis at ambient, retention of some $N(SiMe_3)_2$ groups, and their thermal degradation under reactive conditions of the pyrolysis under an ammonia flow. The residual N-Si-C moieties became the source of Si that could engage a part of Mn, especially if excess of Mn was available, to form by-products in the system Mn-N-Si-C in addition to the target materials in the system Ga-Mn-N. In order to estimate the elemental composition of the powders, X-ray fluorescence XRF determinations were done and the results were normalized for the Ga, Mn, and Si contents. Table 1 contains the results for the 5 and 20 at.% Mn-contents and Table 2 for the 0.1 and 50 at.% Mn-contents.

Table 1. Gallium Ga, manganese Mn, and silicon Si contents derived from X-ray fluorescence determinations for powders with the initial 5 and 20 at.% Mn-contents.

Element X	500 ºC			700 ºC			900 ºC		
	Amount [at.%]	Ga:X	Mn:Si	Amount [at.%]	Ga:X	Mn:Si	Amount [at.%]	Ga:X	Mn:Si
	Initial Mn-content 5 at.% (one-stage pyrolysis) (Ga:Mn = 19:1)								

Ga	94.0	1	-	94.3	1	-	91.8	1	-
Mn	3.9	19.0	-	4.1	18.0	-	4.3	16.9	-
Si	2.1	17.8	0.9	1.6	23,7	1.3	3.9	9,5	0.6
	Initial Mn-content 20 at.% (two-stage pyrolysis) (Ga:Mn = 4:1)								
Ga	84.4	1	-	84.8	1	-	81.6	1	-
Mn	12.7	5.2	-	12.5	5.3	-	13.1	4.9	-
Si	2.9	11.6	2.2	2.7	12.7	2.4	5.3	6.2	1.3

Table 2. Gallium Ga, manganese Mn, and silicon Si contents derived from X-ray fluorescence determinations for powders with the initial 0.1 and 50 at.% Mn-contents.

Element X	900 ºC				
	Initial Mn-content 0.1 at.% (Ga:Mn = 999:1)		Initial Mn-content 50 at.% (Ga:Mn = 1:1)		
	Amount [at.%]	Ga:X	Amount [at.%]	Ga:X	Mn:Si
Ga	99.8	1	73.7	1	-
Mn	0.2	351	21.6	2.7	-
Si	-	-	4.7	6.3	2.3

For the samples with the initial 5 and 20 at.% Mn-contents, the major conclusion is that a majority of the initial Mn, if not all, remains in the powders regardless of the pyrolysis temperature (Tab. 1). The second conclusion is that quite significant quantities of Si are retained as evaluated from the Mn:Si element ratios in the product powders. The initial Mn:Si ratio in $Mn[N(SiMe_3)_2]_2$ is 1:4 or 0.25. If one of the two $N(SiMe_3)$ groups is removed *via* transamination, this ratio will be 0.5. The latter value is close to only one case of 5Mn-900 with Mn:Si equal to 0.6. In all other powders, it is larger than that reaching 2.4 for 20Mn-150/700. This ratio depends to some extent on the applied temperature – it peaks up after pyrolysis at 700 ºC and is the lowest after pyrolysis at 900 ºC. It is a result of a fine interplay between the competing transamination of the $MnN(SiMe_3)_2$ species with removal of volatile silazanes and the thermal decomposition of silazanes moieties with Si retention at increased

temperatures. In conclusion, the data confirm the incomplete ammonolysis/transamination resulting in the competing decomposition of the residual $N(SiMe_3)_2$ groups.

Somewhat different properties are displayed by the system with the extremely large initial proportion of the manganese precursor, *i.e.*, 50 at.% or Ga:Mn=1 (Tab. 2). The product 50Mn-150/900 has the Ga:Mn ratio equal to 2.7 which is consistent with significant losses of manganese. Apparently, such a large starting quantity of $Mn[N(SiMe_3)_2]_2$ caused some unreacted excess of it to sublime out during initial heating stages. Interestingly, the Mn:Si ratio of 2.3 is in the range of 1.3-2.4 seen for the powders from the initial 20 at.% Mn-content indicating, again, similar factors that lead to retention of Si in the products.

The use of the extremely small proportion of $Mn[N(SiMe_3)_2]_2$ of 0.1 at.% (Ga:Mn = 999:1) resulted in the 900 ºC-powder that was analyzed with 0.2 at.% of Mn at the background noise level of the method as applied. This could be the major reason for the relatively large discrepancy between the initial and analyzed Mn-contents.

Powder XRD determinations. Some XRD patterns consisted of extremely broad peaks ("halos") that are typical for nanocrystalline GaN in the low nanosized range. They can be indexed either as the hexagonal h-GaN or cubic c-GaN polytype. In fact, they are characteristic of phase inhomogeneous GaN which can be best described as nanocrystallites made of hexagonal and cubic closed-packed layers.[14,18] In several cases, the deconvolution of patterns by best fitting failed to accommodate for real peak intensities and this was assumed to result mainly from complex texturing/preferential crystallite growth that was often confirmed by SEM examinations. An unusual broadening of peak bases, that was seen in some cases, was attributed to bimodal size distributions, *i.e.*, the presence of larger crystallites and much smaller ones that belonged to two different distribution modes in the nanosized range. However, it is quite possible that this phenomenon is due to specific crystallite texturing, instead. There is also one case (*vide infra*) where very characteristic broadenings of the reflections indicate an extrinsic (double deformation) type of stacking faults present in the 2H GaN lattice as reported earlier by one of the co-authors.[19]

The XRD patterns for the 5 at.% Mn-derived powders (500, 700, and 900 ºC) are presented in Figure 7 and for the 20 at.% Mn-derived powders (500, 700, and 900 ºC) in Figure 8. In Figure 9, the XRD patterns for the extreme compositions are shown, *i.e.*, for the powders prepared at 900 ºC from the initial 0.1 and 50 at.% Mn-contents. Figure 9 includes also the bar charts for hexagonal h-GaN and cubic c-GaN. Table 3 contains the basic structural parameters for the identified phases which were calculated from the XRD data.

The patterns for all three 5 at.% Mn-derived powders (Fig. 7) can be satisfactorily indexed as belonging to the GaN polytypes with bimodal size distributions. No other crystalline phases are discernible. Apparently, the small quantity of Si detected by XRF in these materials (Tab. 1) is either below detection limits of X-ray diffractometry or it is due to amorphous characteristics of the likely N-Si-C-bearing species.

In particular for 5 at.% Mn-contents, powder 5Mn-500 shows a typical "halo" pattern for phase-inhomogeneous, low temperature prepared GaN powders on the verge of crystallinity with an estimated average crystallite size D of 1.5 nm. The pyrolysis at the higher temperature of 700 °C (5Mn-700) results in some c-GaN, D=4 nm, and the major h-GaN, the latter best fitted with two modes of size distribution, D=3 and D=22 nm. After the pyrolysis at 900 °C (5Mn-900), no c-GaN is found and the exclusive h-GaN is characteristic of the

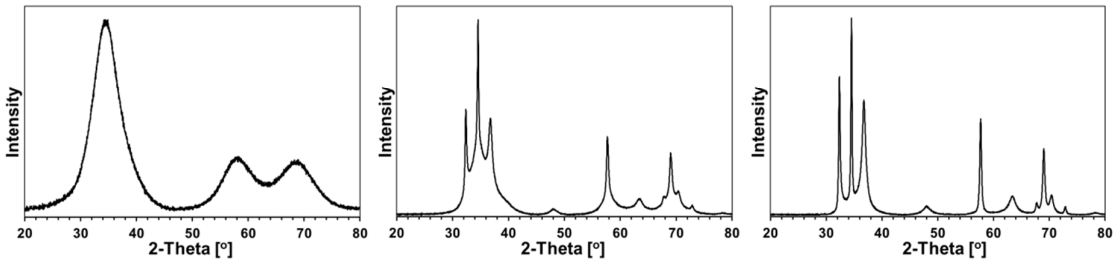

Fig. 7. XRD patterns for powders with initial 5 at.% Mn-content: left – 5Mn-500, middle – 5Mn-700, right – 5Mn-900.

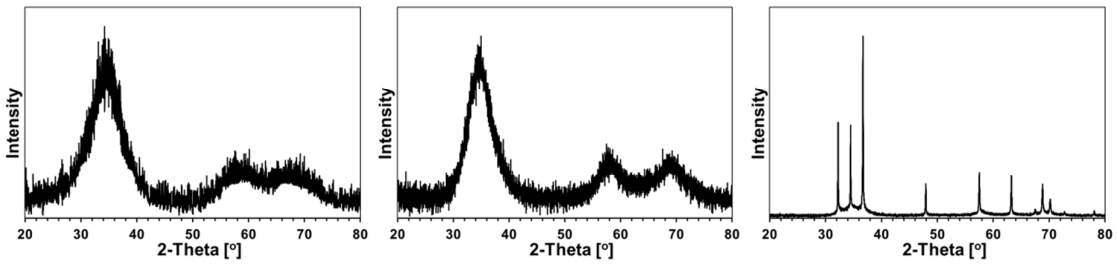

Fig. 8. XRD patterns for powders with initial 20 at.% Mn-content: left – 20Mn-150/500, middle – 20Mn-150/700, right – 20Mn-150/900.

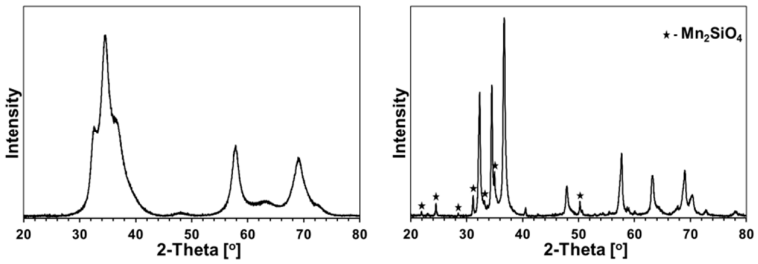

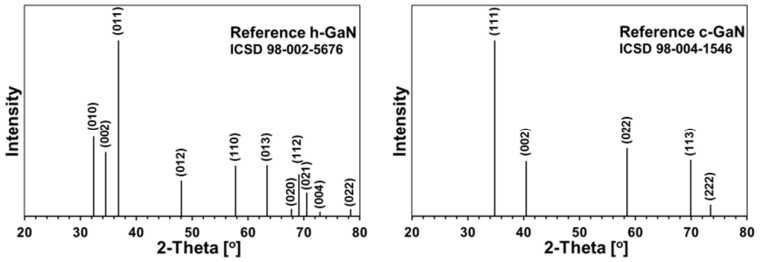

Fig. 9. XRD patterns for powders with the extreme Ga:Mn compositions: upper left – 0.1Mn-150/900, upper right – 50Mn-150/900. The peaks assigned to orthorombic Mn_2SiO_4 are indicated with asterisks. The bar charts in the lower side are for hexagonal h-GaN (ICDD 98-002-5676) – lower left and cubic c-GaN (ICDD 98-004-1546) – lower right.

Table 3. Structural characteristics of GaN-based nanopowders.

Sample	Phase: content [%]	Lattice parameters a[Å], c[Å]	Average crystallite size D [nm]
5Mn-500	c-GaN (phase inhomogeneous): 100	a=4.45	1.5
5Mn-700	c-GaN: 29	a=4.51	4
	h-GaN (large nano): 18	a=3.20 c=5.19	22
	h-GaN (small nano): 53	a=3.19 c=5.27	3
5Mn-900	h-GaN (large nano): 39	a=3.20 c=5.19	36
	h-GaN (small nano): 61	a=3.19 c=5.19	5
20Mn-150/500	c-GaN (phase inhomogeneous): 100	a=4.69	1.1
20Mn-150/700	c-GaN (phase inhomogeneous): 100	a=4.57	1.6
20Mn-150/900	h-GaN (large nano): 44	a=3.20 c=5.19	>100
	h-GaN (small nano): 56	a=3.19 c=5.22	3
0.1Mn-150/900	c-GaN: 54	a=4.52	5
	h-GaN: 46	a=3.20 c=5.29	4
50Mn-150/900	c-GaN: 2	a=4.44	45
	h-GaN: 79	a=3.20 c=5.19	22
	Mn_2SiO_4: 19	-	-

larger average crystallite sizes in the bimodal distribution, D=5 and D=35. These results differ somewhat from the comparable synthesis of pure GaN *via* the same anaerobic route by the appearance of c-GaN in 5Mn-700 and the bimodal size distribution of h-GaN in the powders. This implies specific impact of the Mn-bearing species on GaN crystallization.

The powders with the initial 20 at.% Mn-contents are characteristic of retarded GaN crystallization up to 700 ºC (Fig. 8, Tab. 1). The pattern for 20Mn-150/500 confirms the beginning of crystallization and phase-inhomogeneous GaN, which is typical for the pyrolysis at 500 °C. However, a very similar pattern and the crystallographic features are obtained also for 20Mn-150/700, which is rather surprising and uncommon for GaN powders prepared in this temperature range. Apparently, this is due to a thinning effect that is likely caused by the available residues from decomposition of the remaining $N(SiMe_3)_2$ groups. Pyrolysis at 900 ºC results in the exclusive h-GaN polytype with a bimodal size distribution that includes a fraction of very well crystallized h-GaN, D>100 nm, in addition to a fine fraction with D=3 nm. The SEM images support the formation of both the large elongated microcrystals and the much smaller size homogeneous nanocrystallites, the latter forming blocky agglomerates (Fig. 6, right). In this regard, such small GaN nanocrystallites have not yet been observed by us at this relatively high pyrolysis temperature. Similarly as for the 5 at.% Mn-content, the only phase is that of GaN and the Mn-additive plays a significant role in its crystallization.

Figure 9, left, shows a XRD pattern for the powder prepared with the extremely small proportion of initial Mn of 0.1 at.% upon pyrolysis at 900 ºC. It is worth to note that it is the least crystallized GaN obtained by us in this temperature range over several years of studies on this and related precursor routes to GaN powders. And for the first time, the cubic polytype c-GaN is observed after pyrolysis at 900 ºC in such a high proportion of 54 % (Tab. 3). The average crystallite sizes for c-GaN, D=5 nm, and for h-GaN, D=4 nm, are remarkably low and, certainly, are to be traced to the Mn-additive that even in small quantities has a pronounced impact on GaN crystallization, possibly, through Mn doping.

The initial 50 at.% Mn-content precursor mixture upon pyrolysis at 900 ºC yielded a powder reactive during sample handling in air. The presence of significant quantities of manganese orthosilicate Mn_2SiO_4 (19 %) can be explained by adventitious oxidation of some nanosized or amorphous by-products, which resulted from decomposition of excessive amounts of the manganese precursor. It is worth underlining that this is the only case in the entire study that a crystalline component other than GaN-based polytype(s) is detected by XRD. In addition to Mn_2SiO_4, the product is composed of the major h-GaN in 79 %, D=22 nm, and the minor c-GaN, D=45 nm, the latter in the relatively low amount of 2 %.

Specifically, it can reasonably be argued that Mn_2SiO_4 could have formed by oxidation from such plausible by-products as many of manganese silicides Mn_xSi_y[20] or the binary manganese silicon nitride $MnSiN_2$[21], not to mention very possible transient Mn-N-Si-C species from decomposition of the excess of $Mn[N(SiMe_3)_2]$. In this regard, the oxidation of $Mn_{11}Si_{19}$ in dry oxygen at 800 ºC was found to produce amorphous silica SiO_2 layers on the silicide's surface rather than forming manganese silicate.[22a] As a matter of fact, the so-called silicon monoxide „SiO" was used in reaction with $MnCl_2$ to make Mn_4Si_7 nanowires that were covered with amorphous silica, which supported the propensity of manganese silicides to be oxidized with the preferential formation of amorphous silica.[22b] This picture can be, however, more complex if one considers a prior incorporating by manganese silicide some available carbon to form Mn-Si-C by-products.[23] On the other hand, the presence of N-containing by-products with the Mn-N-Si or Mn-N-Si-C make-up seems to be better substantiated in the reaction system with ammonia. In particular, manganese silicon nitride $MnSiN_2$ was found to be stable up to 1000 ºC and when oxidized with an Ar/O_2 mixture it formed various manganese silicates (rhodonite and braunite) and amorphous silica.[21a]

FT-IR spectroscopy of products. An additional insight is gained from infrared spectra that provide bonding information irrespective of crystallinity, therefore, complementing the powder XRD determinations. The FT-IR spectra for the 5 at.% Mn-derived powders (500, 700, and 900 ºC) are presented in Figure 10 and for the 20 at.% Mn-derived powders (500, 700, and 900 ºC) in Figure 11. The opaque characteristics of the KBr pellets caused occasional deformations of the baseline. The broad bands seen at 3430 and 1630 cm^{-1} are for adventitious water adsorbed during sample handling and KBr pellet preparation.

The common feature in all spectra of the powders with the initial 5 wt.% Mn-content is a strong band at 560-580 cm^{-1} for the Ga-N stretches in GaN [Fig. 10]. Variations in this peak's position in the range *ca.* 550-600 cm^{-1} and its symmetry and broadness for GaN nanopowders are a function of combined experimental as well as materials factors, among them particle size and size distribution, surface properties, oxygen content, crystallinity, present polytypes, and KBr sample turbidity. Interestingly, the spectra for 5Mn-500 and 5Mn-700 also show, respectively, a weak and a very weak band at *ca.* 2070-2090 cm^{-1} that is typical for Si-H stretches and the similar intensity bands at 1400-1500 cm^{-1} for CH_2 deformations.[24] This is accompanied by a medium to a weak intensity band at 950-980 cm^{-1} which is in the range of Si-H deformation mode and Si-N stretches and by medium intensity bands at *ca.* 3150-3400 cm^{-1} and 1600-1620 cm^{-1} assigned to N-H vibrations.[25] These features

are reduced in intensity with increasing pyrolysis temperature and they are absent in the 900 ºC-powder, the latter having a dominant band at 570 cm^{-1} for GaN.

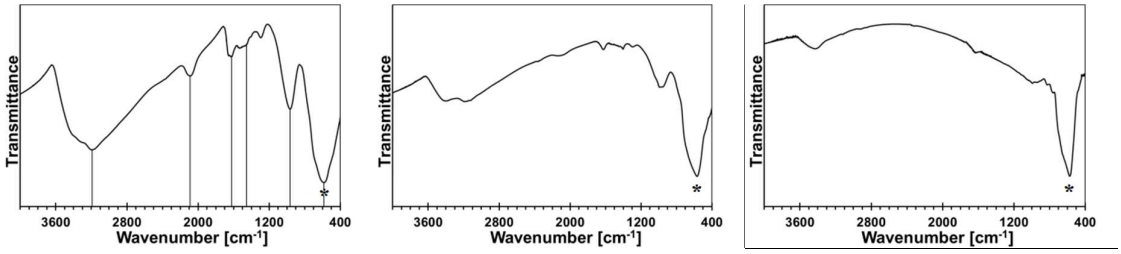

Fig. 10. FT-IR spectra for powders with initial 5 at.% Mn-content: left – 5Mn-500, middle – 5Mn-700, right – 5Mn-900. Asterisks show the Ga-N stretch, vertical lines in the left are guides to the eye for important bands.

The spectral features are consistent with the incomplete transamination chemistry and retention of residual $N(SiMe_3)_2$ groups followed by their decomposition under a reactive ammonia atmosphere. It is known that $SiMe_3$ groups and related polycarbosilanes start to decompose at temperatures as low as 250-300 ºC with the formation of Si-H functionalities, which can persist up to 700-800 ºC.[24] Based on the FT-IR spectra, there are thus indications that the polymeric/amorphous {Mn-N(H)-Si(H)-CH_2-} species are formed at lower pyrolysis temperatures. This agrees well with the XRD/EDX and XRF analyses that confirmed the presence of Si in the powders.

The FT-IR spectra for the powders with the initial 20 at.% Mn-content (Fig. 11) confirm the findings discussed earlier for the 5 at.% Mn-content. It is worth to note that the manganese nitride η-Mn_2N_3, which is otherwise formed in the reaction of pure $Mn[N(SiMe_3)_2]$ and NH_3, is reported to show no active vibrational mode in the mid-infrared range.[17] The relevant bands are now more intense due to the higher proportion of the manganese precursor used in excess and, therefore, higher quantities of the by-products. The dominant band is at 560-570 cm^{-1} for GaN. The Si-H stretch at 2030 cm^{-1} is very intense for 20Mn-150/500, reduced in intensity for 20Mn-150/700, and absent for 20Mn-150/900 after pyrolysis at 900 ºC. There are rather weak bands for the N-H vibrations at 3150-3170 and 1550 cm^{-1}. The spectrum for 20Mn-150/900 is relatively simple and contains the major GaN-related band at 570 cm^{-1} and a weak and broad band extending from *ca.* 800 to 950 cm^{-1} that reflects some amorphous by-products. These qualitative results can be compared with the XRF analyses in Table 1. The ratio Mn:Si is approximately twice as high for the 20 at.% Mn-derived powders compared with the 5 at.% Mn-derived powders.

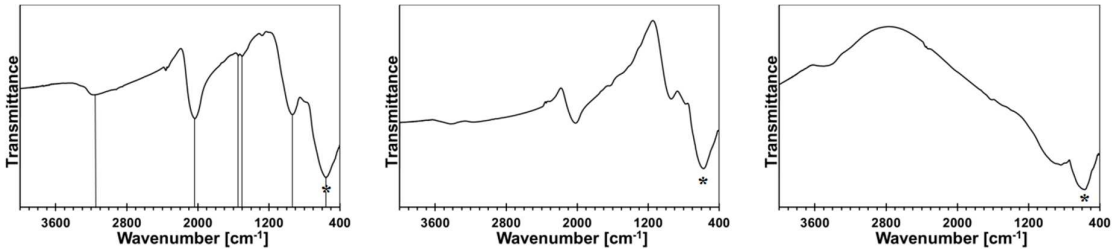

Fig. 11. FT-IR spectra for powders with initial 20 at.% Mn-content: left – 20Mn-150/500, middle – 20Mn-150/700, right – 20Mn-150/900. Asterisks show the Ga-N stretch, vertical lines in the left are guides to the eye for important bands.

The FT-IR spectra for the 0.1 at.% Mn-150/900 and 50 at.% Mn-150/900 powders (not shown) generally display features supporting the presence of the major GaN-based product and some by-products. In this regard, the former powder shows the predominant Ga-N stretch at 580 cm^{-1} whereas the latter specifically indicates that the by-product can be one of manganese silicates – a set of three medium intensity bands at 818, 857, and 945 cm^{-1} match well the strongest bands at 820, 867, and 950 cm^{-1} recorded for mineral tephroite which is orthorhombic Mn_2SiO_4.[26] Based on this evidence and the relevant XRD data (Fig. 9) the 50 at.% Mn-150/900 powder appears to be composed of two crystalline components, *i.e.*, GaN-type phase and Mn_2SiO_4. The latter could result from post-reaction adventitious oxidation of the initially formed decomposition by-products {Mn-N(H)-Si(H)-CH_2}. This is further supported by the XRF data that show for this powder the ratio Mn:Si equal to 2.3 to be compared with such a ratio of 2 in Mn_2SiO_4. In conclusion, the majority of Mn seems to be associated with the air sensitive by-products whereas only part of it may have entered doping reactions with the gallium nitride precursor towards GaMnN.

Raman spectroscopy of products. The Raman spectra for the 700 and 900 °C-derived materials are shown in Figure 12 and the best-fitted bands are listed in Table 4.

Generally, each of four spectra contains a similar set of bands, alas, of varying intensities. The two strongest bands are typical for GaN lattices, *i.e.,* the band in the range 701-718 cm^{-1} is the LO mode in h-GaN and/or in c-GaN whereas the band at 548-561 cm^{-1} is assigned to the E_2 mode in h-GaN and/or TO mode in c-GaN.[27] The rather weak bands at 649-670, 406-417, and 278-301 cm^{-1} are frequently observed in GaN with extensive lattice defects or doped GaN lattices including Mn-doping.[27d] Finally, the weak to very weak features at 400-475 and 244-252 cm^{-1} could not be identified in any of the available reports on Raman studies in related systems and are thus assigned to by-product contaminants. It is instructive to

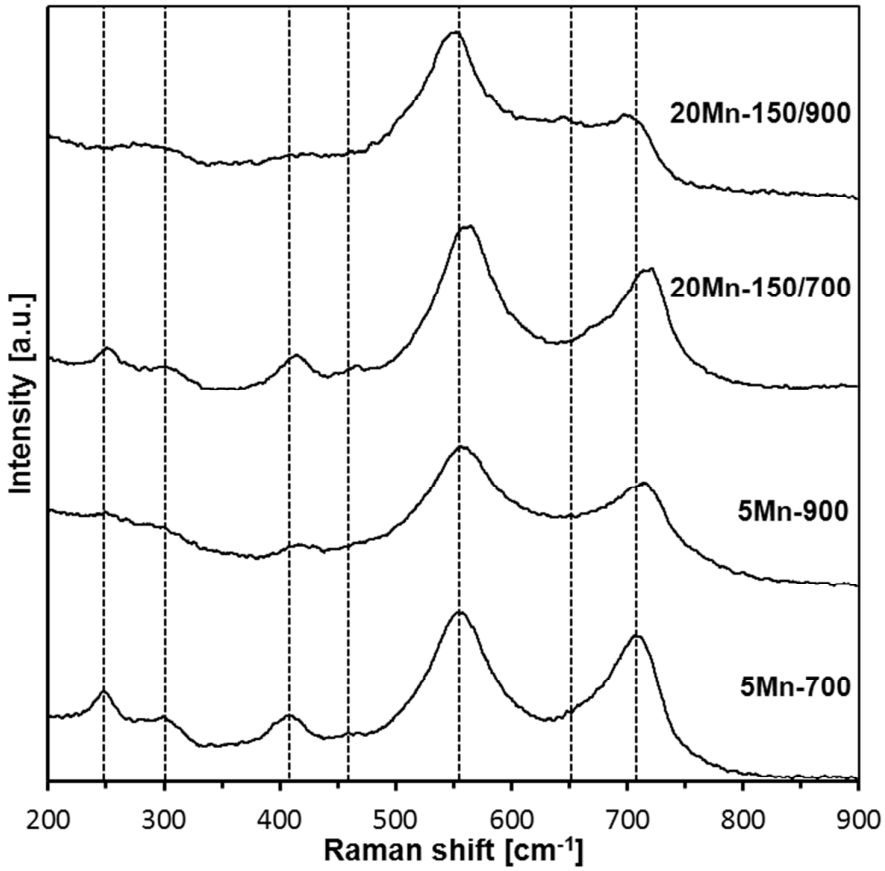

Fig. 12. Raman spectra for 700 and 900 °C-derived nanopowders.

Table 4. Best-fitted Raman shifts for 700 and 900 °C-derived nanopowders.

	5Mn-700	20Mn-150/700	5Mn-900	20Mn-150/900
Assignment	Raman shifts [cm^{-1}] (*sh* – shoulder; *vw* – very weak)			
LO (hexagonal and/or cubic GaN lattices)	709	718	716	701
N-vacancy in doped GaN	660 (*sh*)	670 (*sh*)	660 (*sh*)	649 (*vw*)
E_2 (h-GaN lattice) TO (c-GaN lattice)	555	561	558	548
by-product	466 (*vw*)	460	475 (*sh*)	-
2-phonon difference mode	406	413	417	416
disorder-activated/ acoustic phonon at zone boundary	300	301	300 (*vw*)	278
by-product	247	252	244 (*vw*)	-

relate the major bands to the reported Raman shifts for the pure/undoped GaN powders prepared with the same method and at the same temperatures although measured under different laser irradiation conditions.[28] For the 700 °C-derived pure GaN nanopowder, bands at 332, 410, 550, 637, and 744 cm^{-1} are observed implying lattice defects in GaN. In the 900°C-derived powder, there are mostly bands at 410, 570, and 730 cm^{-1} consistent with much better crystallized GaN. The latter property is also reflected by an enhanced relative intensity of the LO phonon mode[27c] agreeing well with the previously discussed XRD data. Of special interest is also an observation of the shift to lower frequencies for the E_2 and LO modes compared with pure GaN which has been observed on several occasions for Mn-doped GaN/GaMnN.[27e,f] In conclusion, the Raman study is consistent with the synthesis of Mn-doped GaN nanopowders that show improved crystallinity and smaller quantities of contaminants with increased synthesis temperature.

Magnetization measurements. Magnetization of the samples was measured at magnetic fields B up to 7 Tesla in the temperature range 2 K<T<400 K. For all the samples, a diamagnetic contribution of the host GaN material was taken into account. The representative data of magnetization M as a function of magnetic field B at different temperatures are shown for sample 5Mn-150/500 in Figs. 13 and 14, the latter being an expanded high temperature part of the former.

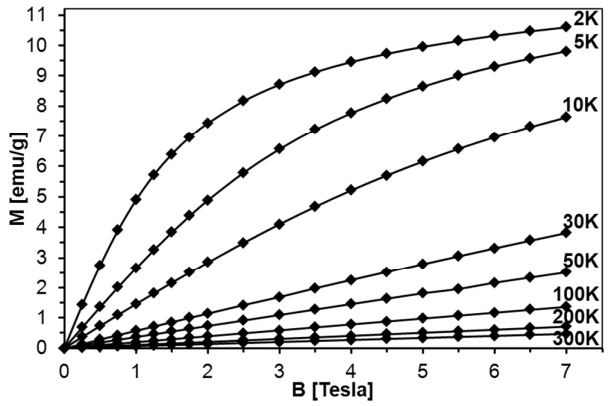

Fig. 13. Magnetization of sample 5Mn-150/500 as a function of magnetic field B at different temperatures. The lines connect experimental points and are guides to the eye, only.

The magnetization reveals rather typical paramagnetic, Brillouin-like behavior: it tends to saturate with increasing B at the lowest temperatures, whereas at higher temperatures (T>100 K) is practically linear with B. Similar behavior is observed for all the samples (Fig. 15) where curves M *vs.* B at T=2 K are shown. It should be noted that the measured

magnetization data do not correlate with the initial Mn-contents used for synthesis. This suggests that only fraction of the used manganese enters the paramagnetic Mn-doped GaN lattice since the observed M(B,T) dependence is typical for GaN doped with Mn.[4,6,29] In this regard, GaMnN grown previously by other techniques usually suffered from ferromagnetic precipitations of Mn_xN_y (or Ga_xMn_y) formed during the growth process.[30] These precipitations manifest themselves by a rapid increase of magnetization at low magnetic fields (B<0.5 T) and are clearly visible at the temperatures T>50 K. A detailed examination of the low field data (Figs. 13-15) shows that our samples are free of such effects. Therefore, one may conclude that the applied synthesis method, in contrast to many previously reported methods for GaMnN growth, produces powders free of ferromagnetic precipitations.

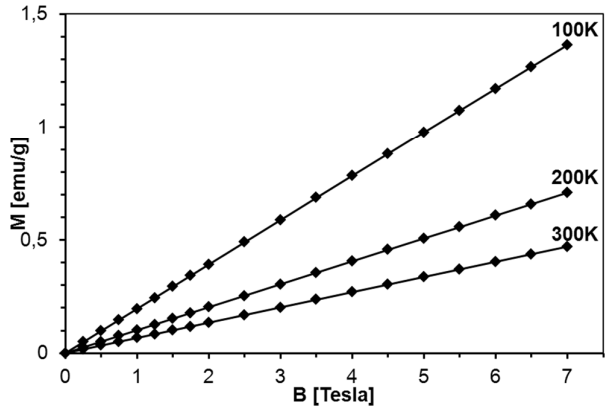

Fig. 14. Magnetization of sample 5Mn-150/500 as a function of magnetic field at T=100, 200, and 300 K. The lines are guides to the eye, only.

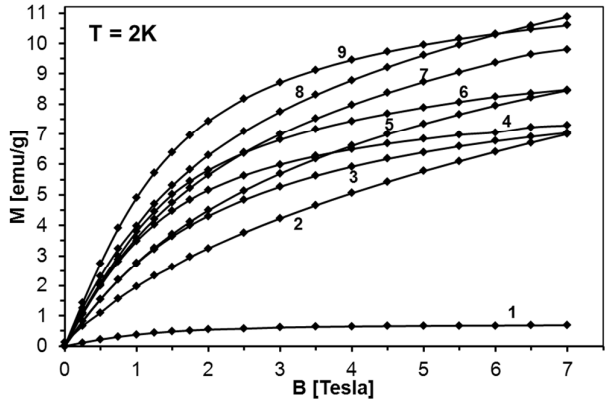

Fig. 15. Magnetization M as a function of magnetic field strength B at T=2 K for selected powders: 1 – 0.1Mn-150/900, 2 – 50Mn-150/900, 3 – 5Mn-900, 4 – 5Mn-500, 5 – 20Mn-150/900, 6 – 5Mn-700, 7 – 20Mn-150/500, 8 – 20Mn-150/700, 9 – 5Mn-150/500. The lines are guides to the eye, only.

It should be noted that magnetization decays with temperature rather slowly, much slower than expected for a typical Brillouin-type paramagnet. This is exemplified in Fig. 16, where magnetization of sample 50Mn-150/900 is shown as a function of temperature, together with function 1/T, pinned to the data at the lowest temperature. The observed behavior suggests that the excess contribution to the magnetization results from yet another magnetic phase neither paramagnetic GaMnN nor a ferromagnetic one.

This observation is farther confirmed if one tries to describe the measured magnetization using a standard method of effective Brillouin function[31], very effectively used in modeling the systems of interacting magnetic ions randomly distributed in nonmagnetic host lattice.[29,31,32] We recall that this formalism assumes magnetization in the form that is shown below in Equation 1.

$$M = Nxg\mu_B SB_S\left(\frac{g\mu_B SB}{k_B(T+T_0)}\right) \quad (1)$$

$$B_S(z) = \frac{2S+1}{2S}coth\left(\frac{2S+1}{2S}\,z\right) - \frac{1}{2S}coth\left(\frac{1}{2S}\,z\right) \qquad z = \frac{g\mu_B SB}{k_B T}$$

where $B_S(z)$ is Brillouin function, N is number of GaN unit cells in 1 g, x is Mn molar concentration, S is the spin of Mn-ion (5/2 in the case of GaMnN), and T_o is effective temperature reflecting interaction between Mn-ions (T_o<0 for FM coupling and T_o>0 for AFM interaction).[31] Typically, N and T_o are adjustable parameters which should provide proper description in the entire temperature range.

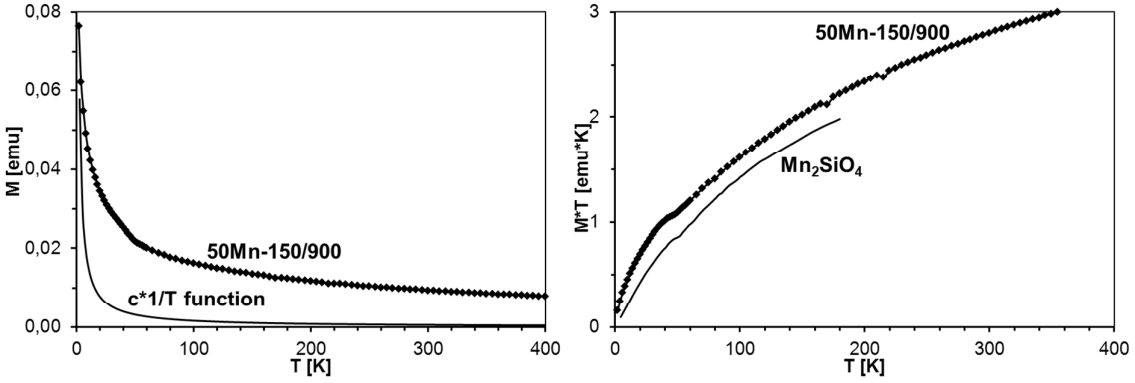

Fig. 16. Left – magnetization of sample 50Mn-150/900 as a function of temperature at B=1 Tesla. The solid line shows c·1/T function, where c was chosen to match the experimental data at T=2 K. Right – M·T *vs.* T plot for sample 50Mn-150/900 and Mn_2SiO_4.[33a]

The sample fit is depicted in Fig. 17 for powder 50Mn-150/900, at T=2 K and 300 K. The fit at 2 K is acceptable although not perfect (x=0.023 and T_0=+3.9 K). However, there is no way to describe the 300 K data with parameters x and T_0 obtained for T=2 K. The calculated magnetization according to Eq. 1 recovers only a small fraction of the measured magnetization.

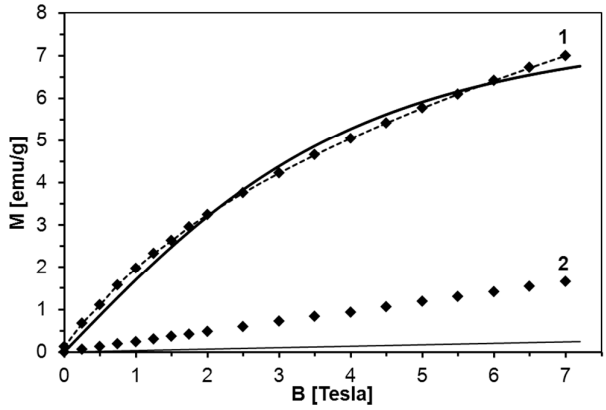

Fig. 17. Magnetization of sample 50Mn-150/900 as a function of magnetic field strength at T=2 K (1) and T=300 K (2). Solid lines depict effective Brillouin function model described in the text: thick solid line – T=2 K, T_o=3.9 K, x=0.023; thin solid line – T=300 K, T_o=3.9 K, x=0.023. Dashed line – Brillouin function complemented by the term b·B.

Apparently, the model of the Mn-ion system incorporated in the GaN lattice cannot satisfactorily describe the measured magnetization only by itself. A part of the measured magnetization must result from a distinct magnetic phase other than homogenous GaMnN. Since this additional magnetic contribution seems to be linear with magnetic field (Fig. 17), does not follow the 1/T decay characteristic for paramagnets (Fig.16), and shows no effects of fast saturation at low fields typical for ferromagnetic phases (Fig.14), we ascribe it to an antiferromagnetic (AFM) phase containing Mn. This phase (or phases) must have been formed during the synthesis. A possible candidate for this phase is Mn_2SiO_4, which can be a likely oxidation by-product in our synthesis and is known to be an antiferromagnet.[33] Moreover magnetization of Mn_2SiO_4 reveals a characteristic bump around 40 K which is also visible in our data (Fig. 16, right). Actually, our XRD study directly confirmed the presence of the orthorhombic Mn_2SiO_4 in powder 50Mn-150/900 (Fig. 9). Having this in mind, the measured magnetization should be the sum of two contributions, *i.e.*, the Brillouin-type contribution described by Eq. 1 and the antiferromagnetic contribution, which can be modeled by a linear function of magnetic field B:

$$M = Nxg\mu_B SB_S\left(\frac{g\mu_B SB}{k_B(T+T_0)}\right) + bB \qquad (2)$$

where x, T_o, and b are adjustable parameters.

Fitting magnetization data with Eq. 2 provides excellent description of the experimental data as shown in Fig. 17. We note that in the case of powder 50Mn-150/900, with the highest initial Mn-content, the antiferromagnetic contribution constitutes more than half of the measured magnetization. The Mn concentration estimated from the Brillouin-like contribution in GaMnN is about 3 at.%. Similar fits for the other powders show that regardless the initial Mn-contents, the actual Mn concentration in GaMnN is found at around 3 at.% with the exception of powder 5Mn-150/500 for which it reaches 3.8 at.%. The rest of Mn that stays in the products seems to form the AFM phase/phases.

For all the samples, T_o is rather small (not larger than 5 K) and positive indicating AFM interactions among Mn-ions in the GaMnN phase. These observations are in agreement with the previous reports on GaMnN for which the nearest neighbor exchange integral was estimated to be J=-1.9 K.[29]

The standard way to demonstrate interactions in the Brillouin-type paramagnetic system is plotting M·T *vs.* T. We recall that for a non-interacting magnetic system one gets a straight horizontal line whereas for an interacting system the line bends at low temperatures (where thermal energy is comparable to exchange coupling): upward for ferromagnetic exchange interactions and downward for antiferromagnetic ones. In the present case, the measured magnetization is the sum of those for GaMnN and for the AFM phase (most probably Mn_2SiO_4), so the M(measured)·T *vs.* T curve is the sum of the M(GaMnN)·T *vs.* T and M(AFM)·T *vs.* T curves as depicted in Fig. 18. The plots of M(measured)·T *vs.* T are shown in Fig. 19 for all four powders prepared from the initial 5 at.% Mn-content precursor. Since at sufficiently high temperatures (T several times larger than T_o, so approx. $T=T+T_o$) the M(GaMnN)·T *vs.* T is a straight horizontal line, the observed increase of M(measured)·T *vs.* T with increasing temperature (Figs. 18 and 19) is due to the AFM contribution M(AFM)·T *vs.* T. Direct subtraction of M(AFM)·T *vs.* T is rather difficult because the actual content of the AFM phase is not known. However, if the functional dependence of M(AFM)·T *vs.* T is known[33c], one can suitably scale it and subtract it in the way that M·T(T) for T>200 K yields a straight horizontal line (Fig. 19, right). For sufficiently small/residual mass of by-product the resulting constant value of M·T (T>200 K) should be proportional to the number of magnetic ions Nx (Eq. 3),

$$MT = Nx\frac{g^2\mu_B^2 S(S+1)}{3k_B} \quad (3)$$

so one can estimate from such a relationship the actual concentration of Mn in the paramagnetic phase GaMnN. The calculated Mn-contents in GaMnN (at.%) and the contents of Mn_2SiO_4 (wt.%) for samples with the initial 5 at.% Mn-contents are depicted in Table 5.

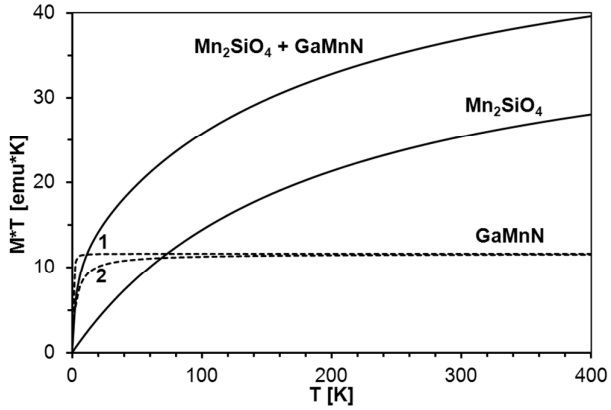

Fig. 18. M·T *vs.* T for: noninteracting magnetic moments in GaMnN (dashed line 1, $T_0 = 0$ K), antiferromagnetically interacting spins in GaMnN (dashed line 2, $T_0 = +3$ K), AFM Mn_2SiO_4, sum of GaMnN and Mn_2SiO_4.

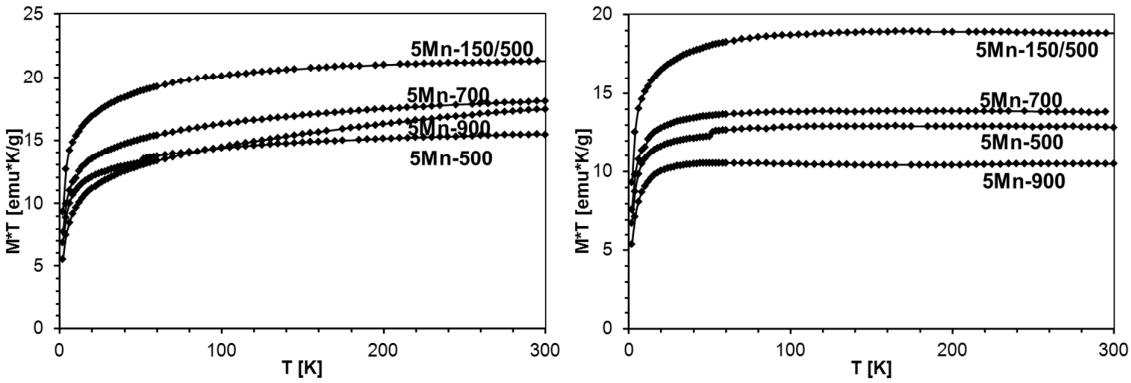

Fig. 19. Left - M·T *vs.* temperature, B=1 Tesla, for various samples with the initial 5 at.% Mn-content. Right - M·T *vs.* T after subtraction of the Mn_2SiO_4 contribution as described in text.

Table 5. Calculated Mn-contents in the paramagnetic phase GaMnN (at.%) and contents of antiferromagnetic Mn_2SiO_4 (wt.%) in powders from precursor with 5 at.% Mn-content.

	5Mn-150/500	5Mn-500	5Mn-700	5Mn-900
Mn-content in GaMnN [at.%]	3.8	2.5	2.9	2.1
wt.(Mn_2SiO_4) / wt.(sample)×100 % [wt.%]	0.5	1.0	1.7	1.4

We also note that in the group of the 5 at.% Mn-samples the highest amount of Mn_2SiO_4 was in 5Mn-700 (1.7 wt.%) whereas the lowest was in 5Mn-150/500 (0.5 wt.%). This is consistent with the view that the additional pyrolysis at 150 °C is efficient in removing more $N(SiMe_3)$ groups than otherwise rendering the associated Mn-centers to be more reactive towards incorporation in the condensing GaN lattice.

The M·T *vs.* T plots for powders prepared from the precursor with the 20 at.% Mn-content are shown in Figure 20 where both the as-measured plots and the AFM-corrected plots are shown. The calculated Mn-contents in GaMnN (at.%) and Mn_2SiO_4 (wt.%) are included in Table 6.

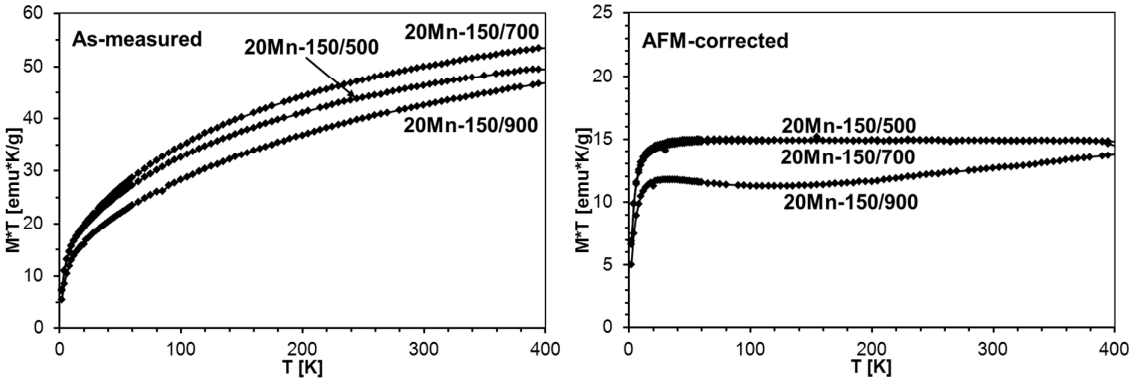

Fig. 20. M·T *vs.* temperature, B=1 Tesla, for powders 20Mn-150/500, 20Mn-150/700, and 20Mn-150/900. The bunch of curved lines on the left side are as-measured plots, the prevailingly flat lines on the right side are AFM-corrected plots.

Table 6. Calculated Mn-contents in the paramagnetic phase GaMnN (at.%) and contents of antiferromagnetic Mn_2SiO_4 (wt.%) in powders from precursor with 20 at.% Mn-content.

	20Mn-150/500	20Mn-150/700	20Mn-150/900
Mn-content in GaMnN [at.%]	3.0	3.1	2.4
wt.(Mn_2SiO_4) / wt.sample)×100 % [wt.%]	6.3	7.0	5.6

As may be seen from comparison of Tables 5 and 6, the concentration of the paramagnetic GaMnN does not seem to depend much on the initial Mn-content and with one exception of 3.8 at.% for 5Mn-150/500 is confined to values in the 2-3 at.% range. On the other hand, the higher initial Mn-content of 20 at.% is associated with significant increases of the antiferromagnetic Mn_2SiO_4 by-product from 1.7 wt.% up to 7 wt.%. The pyrolysis at 700 °C appears to yield the powders with optimal properties – high Mn-contents and chemically stable. Increasing pyrolysis temperature to 900 °C results in the relatively most stable powders but with somewhat reduced Mn-contents in GaMnN in the 2.1-2.4 at.% range. An interesting observation is associated with the potential impact on product/magnetic properties of the first-stage low temperature pyrolysis at 150 °C. The properties of the pair of the related powders, *i.e.*, 5 Mn-500 and 5Mn-150/500, point out to a great significance of this factor and prompt us to an extended study addressing this synthesis aspect to be published elsewhere.

Conclusions

The ammonolysis of the new molecular precursor system made of gallium tris(dimethyl)amide $Ga(NMe_2)_3$ and manganese bis(trimethylsilyl)amide $Mn[N(SiMe_3)_2]_2$, initial Mn-contents from 0.1 to 50 at.%, yields bimetallic precursors that upon nitriding pyrolysis in the range of 500-900 °C result in GaN/Mn nanopowders. They are structurally based on the various GaN lattices as the only crystalline phases and imply Mn-doping towards GaMnN. However, transamination reactions are incomplete under a range of applied compositions and conditions and, consequently, some $MnN(SiMe_3)_2$ groups are retained, later decomposed to amorphous Mn-N-Si-C species that, eventually, may oxidize in air mainly to the manganese orthosilicate Mn_2SiO_4 by-product. The use of the precursors with higher initial Mn-contents causes increased precursor losses due to sublimation during pyrolysis as well as the formation of larger proportions of the residual by-products whereas having no significant impact on the extent of Mn-doping. Some observations linked to low temperature pyrolysis stages offer potentials for further optimization of the synthesis *via* a more efficient ammonolysis towards pure powders.

The results of magnetic measurements confirm the general utility of the applied anaerobic synthesis route for the incorporation of Mn-ions into paramagnetic lattices of GaMnN that are free of FM precipitations typical for other synthesis methods. The effective Mn-concentrations in the GaN lattice are in the range of 2-4 at.%. Attempts to get higher Mn-concentrations by using the bimetallic precursor with increased Mn-contents from 5 to 20 and 50 at.% failed in reaching the goal while yielded higher proportions of the AFM by-product

Mn_2SiO_4, an artefact of an incomplete ammonolysis of the bimetallic precursor. Further work on better tuning the synthesis is in progress including a study on structural and magnetic aspects of high-pressure and high-temperature sintering of such GaN/Mn nanopowders.

Acknowlegements. This study was supported by the Polish National Science Centre – NCN, Grant No. 2011/01/B/ST5/06592. On-call help with the Raman study from Prof. M. Sitarz and Mr. P. Jelen, Faculty of Materials Engineering and Ceramics, AGH-UST, is gratefully acknowledged.

References

1. a) T. Dietl, H. Ohno, *Rev. Mod. Phys.*, 2014, **86**, 187-251; b) T. Jungwirth, J. Wunderlich, V. Novak, K. Olejnik, B. L. Gallagher, R. P. Campion, K. W. Edmonds, A. W. Rushforth, A. J. Ferguson, P. Nemec, *Rev. Mod. Phys.*, 2014, **86**, 855-896; c) A. Hirohata, K. Takanashi, *J. Phys. D - Appl. Phys.*, 2014, **47**, 193001-1-40; d) K. Varaprasad, K. Ramam, G. S. M. Reddy, R. Sadiku, *RSC Adv.*, 2014, **4**, 60363-60370; e) J. M. Li, X. L. Zeng, D. P. Wei, Y. B. Hu, Z. A. Xu, *ACS Appl. Mater. Interfaces,* 2014, **6**, 4490; f) S. S. Khludkov, I. A. Prudaev, O. P. Tolbanov, *Russ. Phys. J.,* 2013, **55**, 903-909; g) J. M. Li, X. L. Zeng, G. Q. Wua, Z. A. Xu, *CrystEngComm*, 2012, **14**, 525.
2. a) J. Borysiuk, P. Caban, W. Strupiński, S. Gierlotka, S. Stelmakh, J. F. Janik, *Cryst. Res. Technol.*, 2007, **42**, 1291-1296; b) J. F. Janik, M. Drygaś, C. Czosnek, B. Pałosz, S. Gierlotka, S. Stelmakh, E. Grzanka, G. Kalisz, A. Swiderska-Środa, M. Leszczyński, G. Nowak, R. Czernecki, *Polish Patent* PL378458, Feb. 29, 2012 (in Polish).
3. For example, see: a) M. Kaminska, S. Podsiadlo, P. Dominik, K. Wozniak, L. Dobrzycki, R. Jakiela, A. Barcz,| M. Psoda, J. Mizera, R. Bacewicz, M. Zajac, A. Twardowski, *Chem. Mater.* 2007*,* **19**, 3139-3143; b) S. Podsiadlo, T. Szyszko, W. Gebicki, J. Gosk, R. Bacewicz, L. Dobrzycki, K. Wozniak, M. Zajac, A. Twardowski, *Chem. Mater.*, 2003, **15**, 4533-4535; c) A. Wolos, M. Palczewska, M. Zając, J. Gosk, M. Kaminska, A. Twardowski, M. Bockowski, I. Grzegory, S. Porowski, *Phys. Rev. B*, 2004, **69**, 115210-7.
4. M. Zając, J. Gosk, E. Grzanka, S. Stelmakh, M. Palczewska, A. Wysmołek, K. Korona, M. Kamińska, A. Twardowski, *J. Alloy. Compd.*, 2008, **456**, 324-338.
5. J. F. Janik, M. Drygaś, C. Czosnek, M. Kamińska, M. Palczewska, R. T. Paine, *J. Phys. Chem. Solids*, 2004, **65**, 639-645.
6. J. B. Gosk, M. Drygaś, J. F. Janik, M. Palczewska, R. T. Paine, A. Twardowski, *J. Phys. D: Appl. Phys.* 2006, **39**, 3717-3725.

7. H. Li, B. Song, H. Q. Bao, G. Wang, W. J. Wang, X. L. Chen, *J. Magn. Magn. Mater.* 2009, **321**, 222-225.

8. Y. Wei, J. Guo, D. Hou, S., *Solid State Commun.*, 2008, **148**, 234-236.

9. U. Kim, H. K. Seong, M.-H. Kim, H. J. Choi, *Mater. Lett.*, 2009, **63**, 97-99.

10. M. H. Ham, J. M. Myoung, *Appl. Phys. Lett.*, 2006, **89**, 173117-1-3.

11. J. F. Janik, R. L. Wells, J. L. Coffer, J. V. St. John, W. T. Pennington, G. L. Schimek, *Chem. Mater.* 1998, **10**, 1613-1622.

12. a) D. C. Bradley, M. B. Hursthouse, K. M. A. Malik, R. Moseler, *Transition Met. Chem.*, 1978, **3**, 253-254; b) H. Chen, M. M. Olmstead, D. C. Pestana, P. P. Power, *Inorg. Chem.* 1991, **30**, 1783-1787.

13. M. Yarema, R. Caputo, M. V. Kovalenko, *Nanoscale*, 2013, **5**, 8398-8410 (and references therein).

14. J. F. Janik, R. L. Wells, *Chem. Mater.,* 1996, **8**, 2708-2711.

15. a) J. F. Janik, E. N. Duesler, R. T. Paine, *Inorg. Chem.,* 1987, **26**, 4341-4345; b) R. T. Paine, J. F. Janik, C. K. Narula, *Mater. Res. Soc. Symp. Proc.,* 1988, **121**, 461; c) J. F. Janik, E. N. Duesler, R. T. Paine, *Inorg. Chem.,* 1988, **27**, 4335-4338.

16. a) K. J. L. Paciorek, J. H. Nakahara, S. R. Masuda, *Inorg. Chem.,* 1990, **29**, 4252-4255; b) F. C. Sauls, W. J. Hurley, L. V. Interrante, P. S. Marchetti, G. E. Maciel, *Chem. Mater.,* 1995, **7**, 1361-1368.

17. M. Drygas, M. M. Bucko, M. Musial, J. F. Janik, *Mater. Chem. Phys.* 2014, *submitted for publication*.

18. J. W. Hwang, J. P. Campbell, J. Kozubowski, S. A. Hanson, J. F. Evans, W. L. Gladfelter, *Chem. Mater.,* 1995, **7**, 517-525.

19. a) J. B. Gosk, *Cryst. Res. Technol.,* 2001, **36**, 197-231; b) J. B. Gosk, *Cryst. Res. Technol.,* 2000, **35**, 101-116.

20. a) A. Pokhrel, Z. P. Degregorio, J. M. Higgins, S. N. Girard, S. Ji, *Chem. Mater., 2013,* **25**, 632-638; b) V. N. Men'shov, V. V. Tugushev, *J. Exp. Theor. Phys.,* 2011, **113**, 121-137.

21. a) R. Pompe, *Thermochim. Acta,* 1976, **16**, 295-300; b) R. Marchand, *C. R. Acad. Sci. C Chim.,* 1971, **272**, 1654-1656; c) M. Kretschmer, *Arch. Eisenhuttenwes.,* 1976, **47**, 15-20.

22. a) L. Stolt, O. Thomas, F. M. d'Heurle, *J. Appl. Phys.,* 1990, **68**, 5133-5139; b) M. H. Ham, J. W. Lee, K. J. Moon, J. H. Choi, J. M. Myoung, *J. Phys. Chem. C,* 2009, **113**, 8143-8146.

23. F. Takanoa, H. Akinaga, H. Ofuchi, S. Kuroda, K. Takita, *J. Appl. Phys.,* 2006, **99**, 08J506-1-3.

24. a) Y. Hasegawa, M. Iimura, S. Yajima, *J. Mater. Sci.,* 1980, **15**, 720-728; b) H. B. Li, L. T. Zhang, L. F. Cheng, Y. G. Wang, Z. J. Yu, M. H. Huang, H. B. Tu, H. P. Xia, *J. Mater. Sci.,* 2008, **43**, 2806-2811.

25. a) D. Su, Y. Li, F. Hou, and X. Yan, *J. Amer. Ceram. Soc.,* 2014, **97**, 1311-1316; b) S. Li, Y. Zhang, *J. Non-Cryst. Solids,* 2012, **358**, 54-57.

26. In „Infrared spectra of mineral species: Extended library", by N. V. Chukanov, Springer Geochemistry/Mineralogy, 2014, **1**, 376.

27. a) W. Limmer, W. Ritter, R. Sauer, B. Mensching, C. Liu, B. Rauschenbach, *Appl. Phys. Lett.*, 1998, **72**, 2589-2591; b) S. N. Waheeda, N. Zainal, Z. Hassan, S. V. Novikov, A. V. Akimov, A. J. Kent, *Appl. Surf. Sci.*, 2014, **317**, 1010-1014; c) X. G. Gao, B. Y. Man, M. Liu, C. Yang, C. S. Chen, C. Zhang, Z. C. Sun, *J. Magn. Magn. Mater.*, 2015, **378**, 447-450; d) M. Zajac, R. Doradzinski, J. Gosk, J. Szczytko, M. Lefeld-Sosnowska, M. Kaminska, A. Twardowski, M. Palczewska, E. Grzanka, W. Gebicki, *Appl. Phys. Lett.*, 2001, **78**, 1276-1278; e) Y. Y. Yu, R. Zhang, X. Q. Xiu, Z. L. Xie, H. Q. Yu, Y. Shi, B. Shen, S. L. Gu, Y. D. Zheng, *J. Cryst. Growth*, 2004, **269**, 270-275; f) L. L. Guo, Y. H. Zhang, W. Z. Shen, *Appl. Phys. Lett.*, 2006, **89**, 161920-1-3.

28. J. L. Coffer, T. W. Zerda, R. Appel, R. L. Wells, J. F. Janik, *Chem. Mater.*, 1999, **11**, 20-22.

29. M. Zając, J. Gosk, M. Kamińska, A. Twardowski, T. Szyszko, S. Podsiadło, *Appl. Phys. Lett.,* 2001, **79**, 2432-2434.

30. M. Zajac, J. Gosk, E. Grzanka, M. Kaminska, A. Twardowski, B. Strojek, T. Szyszko, S. Podsiadło, *J. Appl. Phys.,* 2003, **93**, 4715-4717.

31. J. A. Gaj, R. Planel, G. Fishman, *Solid State Commun.,* 1993, **88**, 927-930.

32. a) R. L. Aggarwal, S. N. Jasperson, J. Stankiewicz, Y. Shapira, S. Foner, B. Khazai, A. Wold, *Phys. Rev. B,* 1983, **28**, 6907-6913; b) A. Twardowski, M. von Ortenberg, M. Demianiuk, R. Pauthenet, *Solid State Commun.,* 1984, **51**, 849-852; c) A. Twardowski, P. Świderski, M. von Ortenberg, R. Pauthenet, *Solid State Commun.,* 1984, **50**, 509-513.

33. a) R. P. Santoro, R. E. Newnham, S. Nomura, *J. Phys. Chem. Solids,* 1966, **27**, 655-666; b) W. Lottermoser, H. Fuess, *Phys. Status Solidi (a),* 1988, **109**, 589-595; c) I. S. Hagemann, P. G. Khalifah, A. P. Ramirez, R. J. Cava, *Phys. Rev. B*, 2000, **62**, R771-R774.